

Technische Universität München  
Physik Department  
E15 Chair for Experimental Physics and Astroparticle Physics



**Bachelor Thesis**

# **Determination of the Specific $^{85}\text{Kr}$ Activity in the Liquid Argon of Gerda Phase II**

Moritz Neuberger

7 August, 2018

Erstgutachter (Themensteller): Prof. S. Schönert  
Zweitgutachter: Prof. H. Kroha  
Betreuer: C. Wiesinger

*"It looks like the neutrinos [...] have mutated into a new kind of nuclear particle."*

– Dr. Satnam Tsurutani in the movie "2012"



# Abstract

The GERmanium Detector Array (GERDA) experiment tries to find evidence for the neutrinoless double beta decay in  $^{76}\text{Ge}$ . Enriched high purity germanium detectors are used simultaneously as source and detector. The liquid argon in which the detectors are located acts as coolant, passive shielding against radiation from the outside and as an active veto due to its scintillation capability. Because of the extremely low background condition, GERDA explores half-lives at about  $10^{26}$  yr. A residual radioactive isotope in the liquid argon is  $^{85}\text{Kr}$ . It does not contribute to the background for GERDA's neutrinoless double beta decay search, but might influence analyses carried out at lower energies. The aim of this thesis is to determine  $^{85}\text{Kr}$ 's specific activity. In about 0.434% the  $^{85}\text{Kr}$  decays are followed by the emission of a gamma with 514 keV. Based on the line count of its peak in the energy spectrum of GERDA, the efficiency in the detectors to measure these gammas and the mean overall measurement time, the specific  $^{85}\text{Kr}$  activity can be calculated. By applying this method, a specific activity of  $(0.508 \pm 0.086)$  mBq/l was determined. A cross-check analysis facilitating the decay lifetime was carried out. However, the presence of  $^{42}\text{Ar}$  with a comparable lifetime did not allow a verification of the obtained result.



# Zusammenfassung

Das GERmanium Detector Array (GERDA) Experiment versucht, Beweise für den neutrinolosen doppelten Betazerfall in  $^{76}\text{Ge}$  zu finden. Angereicherte hochreine Germanium-Detektoren werden gleichzeitig als Quelle und Detektor eingesetzt. Das flüssige Argon, in dem sich die Detektoren befinden, wirkt als Kühlmittel, als passive Abschirmung gegen Strahlung von Außen und als aktives Veto bedingt durch seine Szintillationsfähigkeit. Aufgrund der extrem niedrigen Untergrundbedingung erforscht GERDA Halbwertszeiten bis etwa  $10^{26}$  yr. Ein radioaktives Isotop im flüssigen Argon ist  $^{85}\text{Kr}$ . Es trägt nicht zum Untergrund für die neutrinolose Doppel-Betazerfall-Suche bei, könnte aber Analysen bei niedrigeren Energien beeinflussen. Das Ziel dieser Arbeit ist es, die spezifische Aktivität von  $^{85}\text{Kr}$  zu bestimmen. In ca. 0,434% aller  $^{85}\text{Kr}$ -Zerfälle wird zusätzlich noch ein Gamma mit 514 keV zeitlich verzögert emittiert. Basierend auf der Anzahl an Counts im zugehörigen Peak im Energiespektrum von GERDA, der Effizienz der Detektoren, ein solches Gamma zu messen und auf der mittleren Gesamtzeit kann die spezifische  $^{85}\text{Kr}$ -Aktivität berechnet werden. Durch die Anwendung dieser Methode wurde eine spezifische Aktivität von  $(0.508 \pm 0.086)$  mBq/l bestimmt. Es wurde ein Vergleichsanalyse mit Hilfe der exponentiellen Abnahme der Zählrate durchgeführt. Die Anwesenheit von  $^{42}\text{Ar}$  mit vergleichbarer Lebensdauer erlaubte jedoch keine Überprüfung des erhaltenen Ergebnisses.



# Contents

<b>1</b>	<b>Introduction</b>	1
1.1	Neutrino Physics	1
1.2	GERDA PhaseII	5
1.3	$^{85}\text{Kr}$ Isotope in the Atmosphere	9
<b>2</b>	<b>Line Count Rate Analysis</b>	13
2.1	Preparing the Spectra	14
2.2	Annihilation Peak Suppression	15
2.3	Spectral Fitting	16
2.4	Monte Carlo Simulation	19
2.5	Exposure and Mean Measuring Time	22
2.6	Results	23
<b>3</b>	<b>Change in Count Rate over Time</b>	25
3.1	Plotting the Count Rate over Time	25
3.2	Monte Carlo Simulation	27
3.3	Other Relevant Radioactive Isotopes	28
3.4	Count Rate Fitting	29
<b>4</b>	<b>Conclusion, Comparison and Outlook</b>	31
4.1	Conclusion	31
4.2	Comparison to WARP and Darkside	31
4.3	Outlook	32
<b>A</b>	<b>Detector Overview</b>	33
<b>Bibliography</b>		35



# Chapter 1:

## Introduction

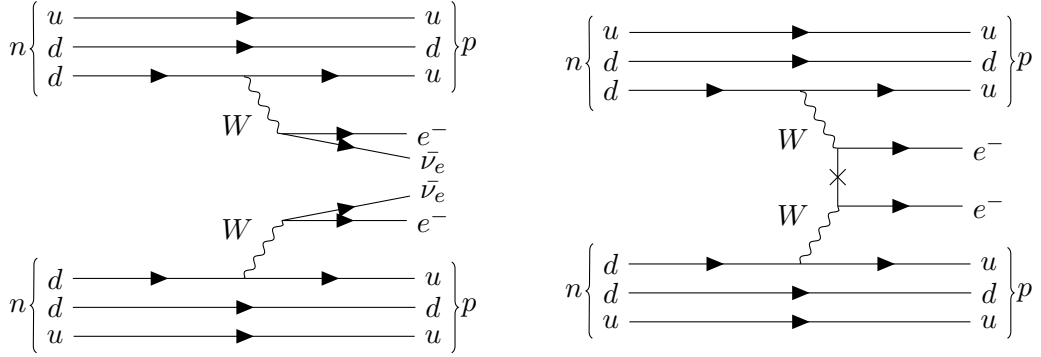
The double beta ( $2\nu\beta\beta$ ) decay has been observed in several isotopes where single beta decay is forbidden. However, the neutrinoless double beta ( $0\nu\beta\beta$ ) decay will only occur when neutrinos are Majorana fermions [1]. Majorana particles have the characteristic of being particle and antiparticle at the same time, breaking the lepton number conservation [2]. The physical background of all this is described in Section 1.1.

The following Section 1.2 will focus on the GERDA experiment. The GERmanium Detector Array (GERDA) experiment tries to find evidence for the neutrinoless double beta ( $0\nu\beta\beta$ ) decay in  $^{76}\text{Ge}$  [3].  $0\nu\beta\beta$  decay is known to have a very long half-life. It is therefore important to minimize background as good as possible. A passive shield around the detectors for suppression of external radiation as well as a scintillator around the detectors to actively reject radiation from the outside are therefore needed. Liquid argon (LAr) is a fitting material for both of these requirements due to its low boiling point, its good shielding characteristics and its ability to scintillate. Commercial argon is extracted from the atmosphere by air liquefaction. Impurities can be removed by cryogenic distillation but traces of radioactive components can be left. One residual radioactive isotope is  $^{85}\text{Kr}$  and will be discussed in Section 1.3.

### 1.1 Neutrino Physics

#### 1.1.1 Neutrinos and Lepton Number Conservation

Neutrinos are electrically neutral elementary particles. They are leptons and, apart from gravity, they only interact with other particles via the weak force. They occur in three different kinds of flavors: the electron neutrino  $\nu_e$ , the muon neutrino  $\nu_\mu$  and the tau neutrino  $\nu_\tau$ . According to the standard model neutrinos would be massless. Neutrino oscillation, however, has shown that neutrinos are massive [4, 5]. But the absolute values of their mass and whether they are Dirac or Majoran particles are



(a) Feynman-Diagram for the  $2\nu\beta\beta$ -decay. Two neutrons transfer into two protons, two electrons and two electron anti-neutrinos. This decay has already been observed in 12 different nuclei [7].

(b) Feynman-Diagram of the  $0\nu\beta\beta$  decay. Two neutrons transfer into two protons and two electrons. In this case the  $0\nu\beta\beta$  decay is due to an exchange of a massive Majorana neutrino. This transition has not been detected yet.

Figure 1.1: Feynman-Diagrams of the  $0\nu\beta\beta$ - and the  $2\nu\beta\beta$ -decay

still unknown.

The major difference between these two kinds of particles is that, in the case of Dirac particles, one can clearly identify particles and anti-particles while Majorana particles only have one kind. In other words, Majorana particles are particle and anti-particle at the same time. This would allow lepton number violation and point towards physics beyond the standard model. Until now, only one possible transition is known that could identify neutrinos as Majorana particles [1]. This transition is referred to as a neutrinoless double beta ( $0\nu\beta\beta$ ) decay.

### 1.1.2 $0\nu\beta\beta$ Decay

The double beta ( $2\nu\beta\beta$ ) decay describes the transition of two neutrons to two protons in the same nuclei. The standard model of particle physics needs two electrons and two electron-antineutrinos in the final state of this process.

$$(A, Z) \rightarrow (A, Z + 2) + 2e^- + 2\bar{\nu}_e \quad (1.1)$$

The corresponding diagram is drawn in Figure 1.1a. It is only observable if a single beta decay is forbidden, while a  $2\nu\beta\beta$  decay is allowed. In most cases, this is due to the fact that the initial state of the nuclei  $(A, Z)$  is stronger bound than the transition state  $(A, Z + 1)$  and less strong than the final state  $(A, Z + 2)$ . Their half-lives are in the order of  $10^{21}$  to  $10^{26}$  yr [6, 7].

In the case of a  $0\nu\beta\beta$  decay, no neutrinos are released:

$$(A, Z) \rightarrow (A, Z + 2) + 2e^- \quad (1.2)$$

From here, it will be assumed that the  $0\nu\beta\beta$  decay is caused by an exchange of massive Majorana neutrinos as seen in 1.1b. A non zero effective neutrino mass  $\langle m_{\beta\beta} \rangle^2$  can be determined from  $0\nu\beta\beta$  decay's half-life  $T_{1/2}^{0\nu}$  when using their interdependence of  $1/T_{1/2}^{0\nu} \propto \langle m_{\beta\beta} \rangle^2$  [8]. This effective neutrino mass is defined by

$$\langle m_{\beta\beta} \rangle = \left| \sum_i U_{ei}^2 m_i \right| \quad (1.3)$$

The PMNS mixing matrix elements  $U_{\alpha i}$  originate from neutrino flavor mixing. Neutrino oscillation experiments have shown that neutrino flavor eigenstates  $\nu_\alpha$  that couple to the W boson are a superposition of neutrino mass eigenstates  $\nu_i$  [4, 5].

$$|\nu_\alpha\rangle = \sum_i U_{\alpha i}^* |\nu_i\rangle \quad (1.4)$$

The elements of the matrix are defined by three mixing angles and three CP-violating phases. The Dirac phase is always present, regardless whether the neutrino is a Majorana or Dirac particle. The two Majorana phases only have a physical meaning for Majorana neutrinos. Neutrino oscillation is only sensitive to the mass square differences  $\Delta m_{ij}^2 = m_i^2 - m_j^2$  of the mass eigenstates and so far only an absolute value of  $\Delta m_{32}^2$  could be determined. This leaves three different possible scenarios to be considered in the  $0\nu\beta\beta$  decay [9]:

1. normal hierarchy ( $m_1 < m_2 < m_3$ )
2. inverted hierarchy ( $m_3 < m_1 < m_2$ )
3. quasi-degenerate hierarchy ( $m_1 \approx m_2 \approx m_3$ ) in which the mass eigenvalues are much larger than the mass square differences

The effective neutrino mass as a function of the lightest mass of each mass ordering can be seen in Figure 1.2. A  $0\nu\beta\beta$  decay may provide new knowledge about the mass ordering, the mass scale as well as the Majorana phases.

Other attempts to determine the mass of the electron neutrino measure the endpoint of beta decay [10]. A promising experiment right now is the KATRIN experiment. The absolute mass these kinds of experiments can measure, is an incoherent mass sum as seen in equation 1.5.

$$\langle m_\beta \rangle = \sqrt{\sum_i |U_{ei}|^2 m_i^2} \quad (1.5)$$

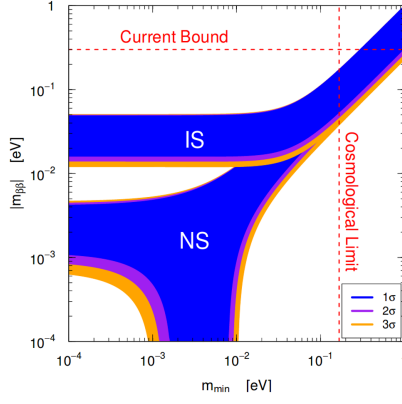


Figure 1.2: Effective neutrino mass  $\langle m_{\beta\beta} \rangle$  as a function of the smallest mass of the respective mass ordering. NS stands for the normal ordering and IS for the inverted ordering. Taken from [12].

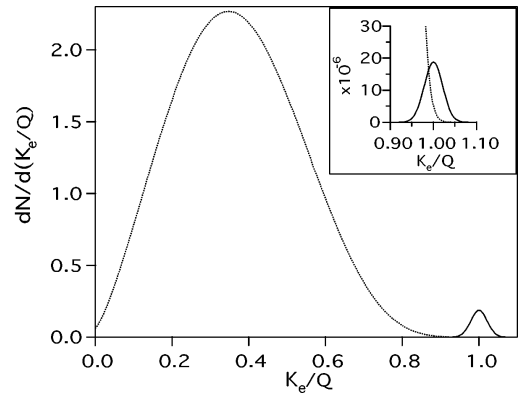


Figure 1.3: Effective spectrum of a  $2\nu\beta\beta$  decay when adding the energies of the two escaping electrons. In case the  $0\nu\beta\beta$  decay occurs a peak can be seen at  $Q_{\beta\beta}$ . Taken from [13].

A third method involves cosmological observation in which the sum of the neutrino masses  $\Sigma$  can be measured [11]:

$$\Sigma = \sum_i m_i \quad (1.6)$$

These three observable give complementary information and might allow to disentangle the Majorana phases, the individual masses of the mass eigenstates and therefore also the mass order of the neutrinos.

### 1.1.3 Experimental methods to detect a $0\nu\beta\beta$ decay

The experimental signature of the  $0\nu\beta\beta$  decay is a sharp peak at the  $Q_{\beta\beta}$  value of the  $2\nu\beta\beta$  decay in the effective spectrum of the two electrons (see Figure 1.3). One experimental approach consist in using a detector made of material enriched in a  $0\nu\beta\beta$  decaying isotope. This has the advantage that the detection efficiency is maximized.

Since  $0\nu\beta\beta$  decay should have a very long half-life, any background has to be minimized just to measure the resulting influence. There are three kind of background sources which have to be considered.

1. Cosmic background. Muons and other particles shower down to the earth from the atmosphere and create background in the detectors. Most of their influ-

ence can be suppressed by placing the experiment deep underground. By also applying a muon veto system most of the residual muon flux can be suppressed.

2. Natural radioactivity. This is typically the dominant background source originating from radioactive isotopes which are naturally present in all materials. Its influence can be suppressed by passively shielding the detectors and by the selecting low radioactive components in the setup.
3. The  $2\nu\beta\beta$  decay material itself. Its impact on the background cannot be reduced by external measures or shielding. However, by using a detector with high energy resolution or a decay material of high Q-value, its influence can be suppressed.

$^{76}\text{Ge}$  has often been used in  $0\nu\beta\beta$  decay search experiment. As it is a semiconductor, it can be used as detector material itself. A disadvantage of  $^{76}\text{Ge}$  is its comparably low Q-value of  $Q_{\beta\beta} = 2039$  keV, which is lower than  $^{208}\text{Tl}$ 's and  $^{214}\text{Bi}$ 's end point energy. It is also hard to increase the target volume compared to e.g.  $^{136}\text{Xe}$  [7]. Its advantages, however, are its ability to be made with great intrinsic radio-purity, its high energy resolution and its high detection efficiency. The possibility to carry out a background-free  $0\nu\beta\beta$  search [3] out weighs this disadvantage.

## 1.2 Gerda Phase II

### 1.2.1 Experimental Setup

The GERDA experiment is located in the underground Laboratori Nazionali del Gran Sasso (LNGS) of INFN, Italy. The laboratories are located approximately 1.4 km below ground, which corresponds to a water equivalent of 3.5 km. GERDA uses  $^{76}\text{Ge}$  as  $0\nu\beta\beta$  source as well as the detector material [3].

The high purity germanium detectors are operated bare in a liquid argon (LAr) tank of  $64 \text{ m}^3$  volume at an working temperature of about 90 K. Its main purpose is to cool the germanium detectors down to their working temperatures and to passively shield them against external radiation originating from the outside. LAr can also scintillate. This is why in Phase II, extra instrumentation was positioned inside the LAr tank in order to measure any light signal around the detectors. As any  $^{76}\text{Ge}$  decays is unlikely to create scintillation light, their signal can be used as a veto - the so-called LAr veto. Situated around the LAr cryostat is a  $590 \text{ m}^3$  water tank. Its main purpose is to shield the setup from outside radiation not only passively by absorption but also actively as a muon veto. Situated in the water tank are 66 photomultipliers. They detect Cherenkov light created by Muons. Above the

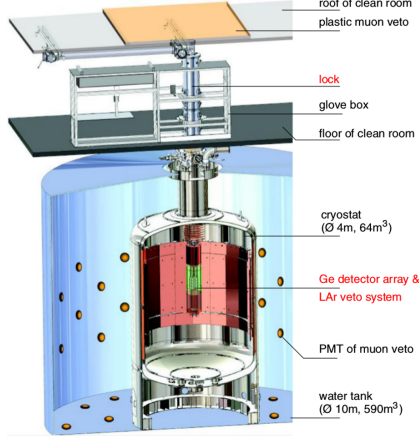


Figure 1.4: Sketch of the GERDA Phase II's experimental setup. The germanium detector array is placed inside a liquid argon (LAr) cryostat which itself is surrounded by a water tank. Taken from [3].

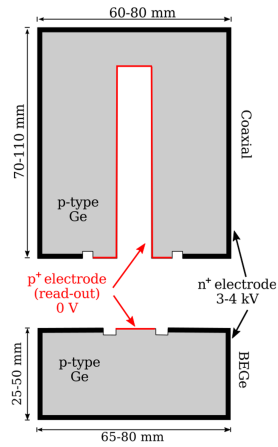


Figure 1.5: Sketch of the Semi-Coaxial (COAX) and Broad Energy Germanium (BEGe) detector designs. Taken from [14].

water tank, a clean room is installed in which the detector strings are assembled [3]. The general setup can be seen in Figure 1.4.

Regarding the detectors themselves, GERDA Phase II uses seven semi-coaxial detectors (COAX) which have already been used in the predecessor experiments (Heidelberg-Moscow and IGEX) as well as 30 new Broad Energy Germanium detectors (BEGe). Both detector types are made of germanium that has been enriched from 7.8% of  $^{76}\text{Ge}$  to about 87%. They also share the same basic functionality. They are made from p-type germanium material. Both detectors have doped most of their surface 1-2mm thick  $n^+$  and only a small part  $p^+$  with both layers to be used as electrodes. If an electron hole pair is created in the p doped area, the charge carriers are separated and guided to the  $n^+$  or the  $p^+$  layer respectively by a strong electrostatic field (3 to 4 kV) between the electrodes. If the pair is created in the  $n^+$  layer, the hole is most likely to recombine in the  $n^+$  layer due to its low mobility and, thus, creates no measurable signal. The  $n^+$  layer is therefore not active and called a dead layer [15].

The two detector types differ in their design as seen in Figure 1.5. Moreover the detector types also differ in their mass and energy resolution. The COAX detector's design results in a worse energy resolution due to their higher capacity compared

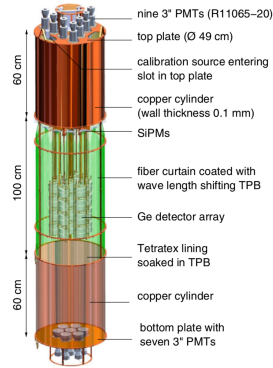


Figure 1.6: Sketch of the liquid argon (LAr) veto setup. In the setup 16 photomultiplier tubes (PMT) and 90 silicon photomultipliers (SiPM) are installed. Taken from [18].

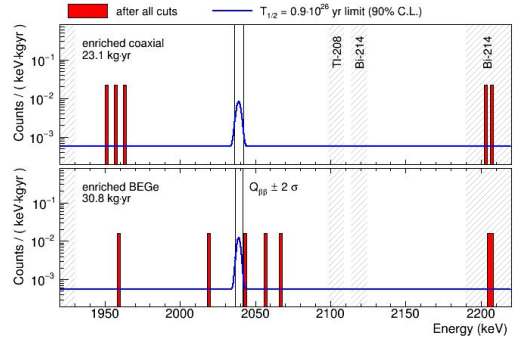


Figure 1.7: Recent results from GERDA Phase II. The measured spectra in the range around  ${}^{76}\text{Ge}$ 's  $Q_{\beta\beta}$  value are displayed separately for the detector type in which the event was measured. Taken from [19].

to the BEGes [15]. BEGes also allow for better pulse shape discrimination (PSD) compared to the COAX detectors. PSD allows to make a statement about the event topology inside the germanium crystal and acts as a veto [16].

The enriched detectors are assembled into 6 strings forming a hexagonal array together with a seventh string. This seventh string consists of three extra coaxial detectors made of natural isotopic germanium. However, they are not used in GERDA's main analysis. Custom-made amplifiers also located in the liquid argon above the detectors. The analog signals of the detectors are digitized at a sampling rate of 100MHz if a triggering signal was found [17]. Every 20 seconds a charge pulse, called the test pulse, is injected into the front-end electronics. Its purpose is to monitor the gain stability. The analysis of the signals is performed off-line. Surrounding the detectors so-called nylon mini shrouds (NMS) are attached to limit the amount of LAr volume around the detectors. These NMS are placed there to passively suppress the background created from  ${}^{42}\text{K}$  [14].

### 1.2.2 Liquid Argon as Coolant, Shielding and Scintillator

LAr is a good coolant due to its low boiling point, also because it corresponds to the operating temperature of the HPGe detectors. In GERDA, it is at about 90 K. LAr can also be produced with a very high purity by air separation and further distillation. It also has good shielding capabilities of radioactive background. It is therefore fitting to be used in GERDA as coolant and ultra pure shielding material [3]. Compared to other noble gases, argon also has the advantage of a rather low

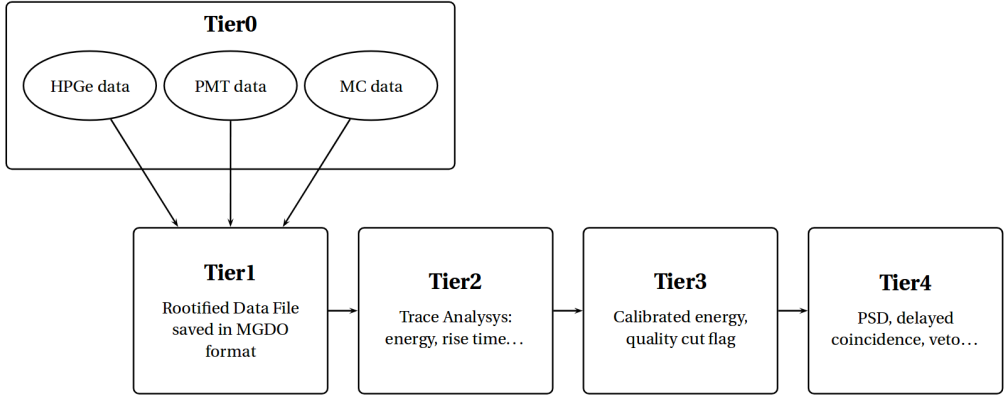


Figure 1.8: The multi-tier structure used by GELATIO. Tier0 and Tier1 contain the entire raw data with the difference that Tier1 already stores the data in a root structure. Tier2, Tier3 and Tier4 contain the resulting data of the successive analysis steps. Taken from [22].

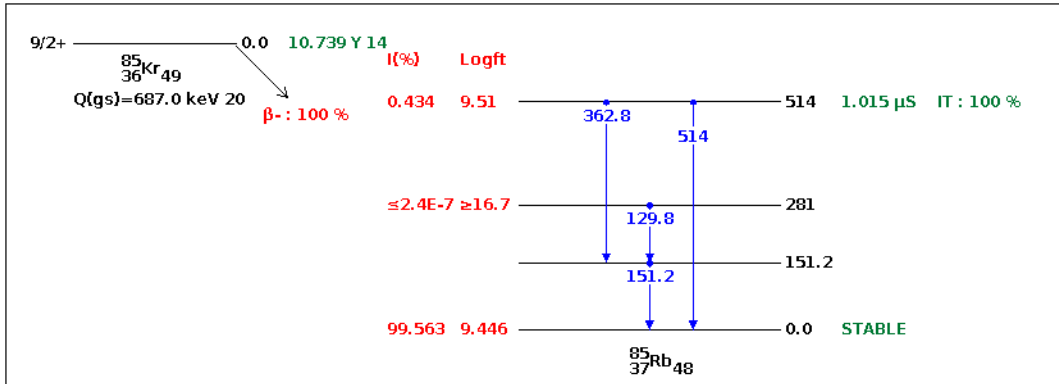
price being easily obtained by liquefaction of air from the atmosphere [20].

LAr has the property that scintillation light is produced when radiation excites or ionizes atoms in the material. The excited atoms in noble liquids form dimer pairs ( $\text{Ar}_2^*$ ). These dimer pairs are metastable and relax with the release of a vacuum ultraviolet photon (VUV) which has a wavelength of 128 nm [20].

Background events often deposit energy in the argon while passing through it. Their scintillation light around the detectors can therefore be used as a veto to reject those events. The LAr veto system consists of a cylindrical copper shell around the germanium detectors and is equipped with 16 photomultiplier tubes (PMT), situated at the bottom and at the top of this volume. Also, at the level of the detectors the shell is not made of copper but of wavelength shifting fibers. These are read out by 90 silicon photomultipliers (SiPM) (see Figure 1.6). VUV has a wavelength which is so small most material absorbs it in ionization. This is why wavelength shifting material covers the surface of the LAr veto shifting from 128nm to about 400nm [21].

### 1.2.3 Data Processing and Analysis

As already mentioned, in the case of an event the digitized signals of the germanium detectors and the LAr channels are stored for further off-line analysis. The software used for the analysis is Gerda LAyouT for Input/Output (GELATIO) being an


 Figure 1.9: The decay scheme of  $^{85}\text{Kr}$ . Taken from [24].

analysis framework specialized for this task. An advantage of it lies in its multiple level data organization as seen in Figure 1.8. Tier0 and Tier1 store the raw data measured by the detectors, while all higher tiers contain the resulting data of the successive analysis steps. Additional information about the analysis process can be found in [22] and [23]. In this thesis only data from Tier3 and Tier4 are used.

To ensure an unbiased approach to the analyzing process, all events measured in a 50 keV interval around  $Q_{\beta\beta}$  were only stored without any analysis applied on them. Only after all parameters were finally defined all events are processed. Such a procedure is called a blinding process.

#### 1.2.4 Recent Results

Only recently, new data was published by GERDA. Only one event in the proximity of the Q-value was found as shown in Figure 1.7, however, it is more than 2 sigma from the expected  $0\nu\beta\beta$  peak position. The conclusion was therefore that no evidence for a  $0\nu\beta\beta$  decay has been seen. A new median sensitivity for setting the lower limit was determined to be  $1.1 \times 10^{26} \text{ yr}$  (90% CL) [19]. Currently GERDA receives an upgrade and is planned to measure until 2020. After that, the successor experiment LEGEND is planned to further investigate the  $0\nu\beta\beta$  decay in  $^{76}\text{Ge}$ .

### 1.3 $^{85}\text{Kr}$ Isotope in the Atmosphere

$^{85}\text{Kr}$  has a mass number of  $A = 85$  and an atomic number of  $Z = 36$ . This isotope is not stable and decays via a  $\beta^-$ -decay into  $^{85}\text{Rb}$ . The half-life of this decay is 10.756 yr and has a Q-value of  $Q_\beta = 687$  keV.  $^{85}\text{Kr}$ 's  $\beta$ -decay has two different

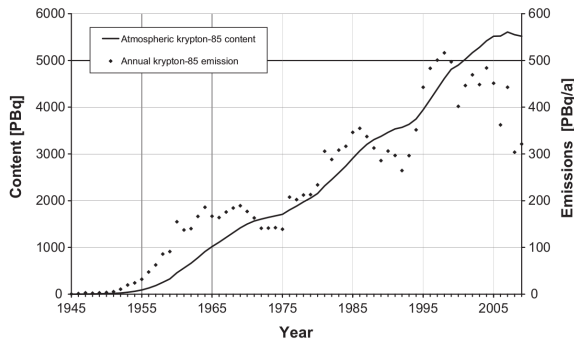


Figure 1.10:  $^{85}\text{Kr}$ 's specific activity in the atmosphere between 1945 to 2009. Over this period the average specific activity in the atmosphere has increased due to man-made nuclear fission in reactors. Taken from [26].

probable transitions (see Figure 1.9). With overwhelming 99.563%, the  $^{85}\text{Kr}$  decay directly populates the ground state of  $^{85}\text{Rb}$ . In 0.434%, however, it decays via an excited state of  $^{85}\text{Rb}$  514 keV above the ground state. This excited state has a half-life of 1.015  $\mu\text{s}$  and relaxes into the ground state while emitting a photon carrying the energy difference [25].

The argon used in GERDA PhaseII was extracted from the atmosphere. By separating argon from the other components of the air, it can easily be made very radioactively pure. Nevertheless, a very small portion of alien elements like krypton can still be present in the extracted argon and therefore also  $^{85}\text{Kr}$ .

When investigating on how  $^{85}\text{Kr}$  got into the atmosphere, two different sources on earth can be identified. On the one hand side, it can be created naturally in the atmosphere by an interaction of  $^{84}\text{Kr}$  with cosmic rays. On the other hand, the production of man-made  $^{85}\text{Kr}$  from nuclear fission of  $^{235}\text{U}$  and  $^{239}\text{Pu}$  generates an atmospheric inventory which is about four orders of magnitude higher. Natural production in the earth's crust is only marginal [27]. Krypton is a noble gas and therefore easily diffuses through everything in its way. It rises until it reaches the atmosphere where a  $^{85}\text{Kr}$  reserve is built over time. Due to the higher amount of nuclear power plants built in the last half century, the  $^{85}\text{Kr}$  activity in the atmosphere has risen to about 5500 PBq in 2009 [26] (see Figure 1.10) .

Two other experiments also using LAr are the WARP and the Darkside experiment. In both experiments the specific activity of residual  $^{85}\text{Kr}$  in the LAr was determined. The Darkside experiment, using underground argon (UAr), has measured a specific activity of  $(2.86 \pm 0.18)$  mBq/l [28]. This UAr has been extracted from underground

reservoirs and should only have come into contact with  $^{85}\text{Kr}$  from natural processes. In the LAr of the WARP experiment, a specific  $^{85}\text{Kr}$  activity of  $(160 \pm 130)$  mBq/l was measured [29]. The WARP experiment uses atmospheric argon which could be the reason why it has a higher specific activity compared to Darkside. The aim of this thesis is to determine the specific  $^{85}\text{Kr}$  activity in the LAr of GERDA Phase II.



## Chapter 2:

# Line Count Rate Analysis

This method to determine the specific  $^{85}\text{Kr}$  activity in GERDA Phase II uses the 514 keV line count rate of the  $^{85}\text{Kr}$  decay. As discussed in Section 1.3,  $^{85}\text{Kr}$  has a small probability of  $p = 0.434\%$  to decay into an excited state of  $^{85m}\text{Rb}$ . When  $^{85m}\text{Rb}$  relaxes into its ground state, it emits a photon of 514 keV energy. The counts  $N_{\text{peak}}$  in the 514 keV line in the GERDA spectra would therefore allow to draw a conclusion concerning the amount of  $^{85}\text{Kr}$  in the LAr, as will be discussed in Sections 2.1 to 2.3.

A factor necessary for the calculation is the efficiency of the germanium detector used to detect these 514 keV gamma. For this, a Monte Carlo simulation is needed in which  $N_{\text{sim}}$  gammas with an energy of 514 keV in a volume  $V_{\text{sim}}$  are simulated. The detector efficiency for 514 keV gammas can then be calculated from dividing the simulated line count at 514 keV by the total number of decays ( $\epsilon = \Delta N/N_{\text{sim}}$ ). The value  $1/p\epsilon V_{\text{sim}}$ , using the detector efficiency, the simulated volume and the probability  $p$  is a conversion factor from a measured line count to the density of decays necessary to create this signal and will be calculated in Section 2.4.

The final value needed is the mean measuring time  $\bar{t}$ . Not every detector was operational over the course of Phase II. This is why an average measuring time for all detectors will be calculated in Section 2.5. With these three values, a mean specific activity  $\bar{a}$  as will be shown in Section 2.6.

$$\bar{a} = N_{\text{peak}} \times \frac{1}{p\epsilon V_{\text{sim}}} \times \frac{1}{\bar{t}} \quad (2.1)$$

The line count rate analysis is expected to generate a relatively precise estimation of the specific activity. This is due to the 514 keV line being a clear feature which can only be traced back to  $^{85}\text{Kr}$ .

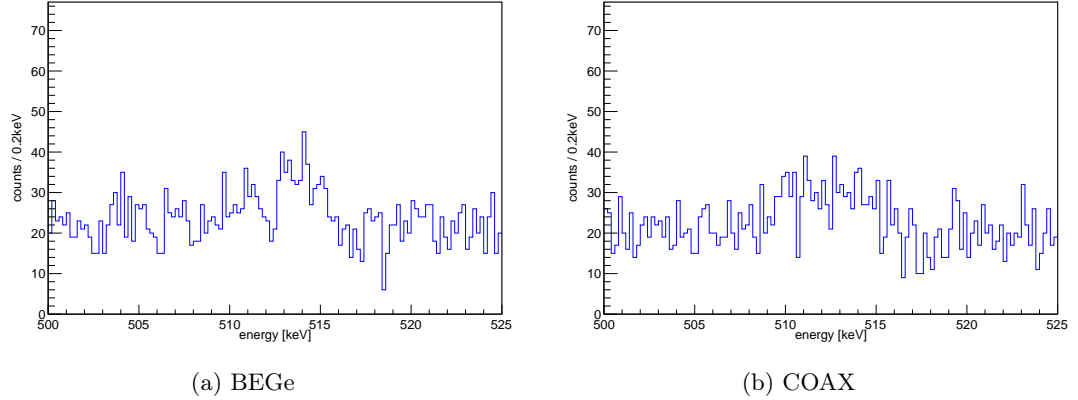


Figure 2.1: Energy spectra after standard GERDA analysis cuts between 500 and 525 keV, split by the respective detectors in which the signal was measured. Two deviations from the background level can be seen in both Figure at 511 keV and 514 keV.

## 2.1 Preparing the Spectra

The data used in this analysis is the fully available GERDA Phase II data (runs 53 to 92). The standard GERDA analysis cuts were applied. This includes data quality cuts, the Muon veto cut and the anti-coincidence cut between germanium detectors.

The data was also split for the two detector types in GERDA. This is necessary due to the differences in detector efficiency and resolution already mentioned in Section 1.2.1. BEGe detectors have a lower efficiency to detect full 514 keV gammas but show a higher energy resolution ( $\sigma_{\text{BEGe}} = 0.96 \text{ keV}@514 \text{ keV}$ ) and vice versa for the COAX detectors ( $\sigma_{\text{COAX}} = 1.16 \text{ keV}@514 \text{ keV}$ ) [3]. The exposure of all BEGe detectors over the entire period of Phase II is 30.8 kg·yr and 28.1 kg·yr for the COAX detectors, calculated in Section 2.5.

Figures 2.1a and 2.1b show the two resulting spectra for each detector between 500 and 525 keV. Structures deviating from the background level can be identified at 511 keV and 514 keV. The 511 keV deviation originates from gammas generated in positron electron annihilation events, while the 514 keV line was most likely caused by gammas created in the relaxation of  $^{85m}\text{Rb}$  in the  $^{85}\text{Kr}$  decay via this excited state. If one examines these figures, one can already make the statement that there must be a not insignificant amount of  $^{85}\text{Kr}$  in the LAr as otherwise no deviation should be visible.

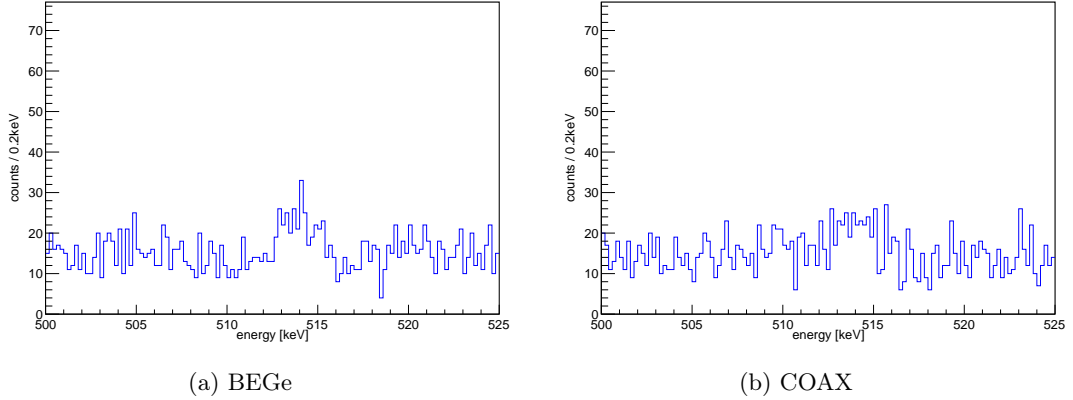


Figure 2.2: Energy spectra after standard GERDA analysis cuts and LAr veto between 500 to 525 keV. The LAr veto made the 511 keV deviation almost completely disappear while the 514 keV deviation is still clearly visible.

## 2.2 Annihilation Peak Suppression

Due to the occurrence of the 511 keV peak, two different approaches are possible. One approach would directly apply a double Gaussian peak fit function to the spectra also fitting the 511 keV peak. Another approach would try to suppress the 511 keV peak and fit a single peak function through the resulting spectra. Both approaches will be applied in this thesis.

A promising candidate in order to suppress the peak, is the LAr veto. It is triggered in the case an event in the germanium detectors coincides with a scintillation signal of at least 0.5 phe [3]. The  $^{85}\text{Kr}$  decay into the excited  $^{85m}\text{Rb}$  leaves the escaping electron with a maximum of 173 keV which should only create a very weak scintillation light signal. Any process involving positron annihilation, however, should create a measurable scintillation light signal visible to the LAr veto setup. Therefore, the LAr veto should be able to discriminate between  $^{85}\text{Kr}$  gamma events and positron annihilating events.

Figures 2.2a and 2.2b show the energy spectra after the LAr veto. One can see that the annihilation peak is reduced compared to the spectra before the LAr veto.

In order to have a better visualization which events have been rejected, all events that triggered the LAr veto are plotted in Figures 2.3a and 2.3b. One can see that the majority of the filtered events had an energy around 511 keV.

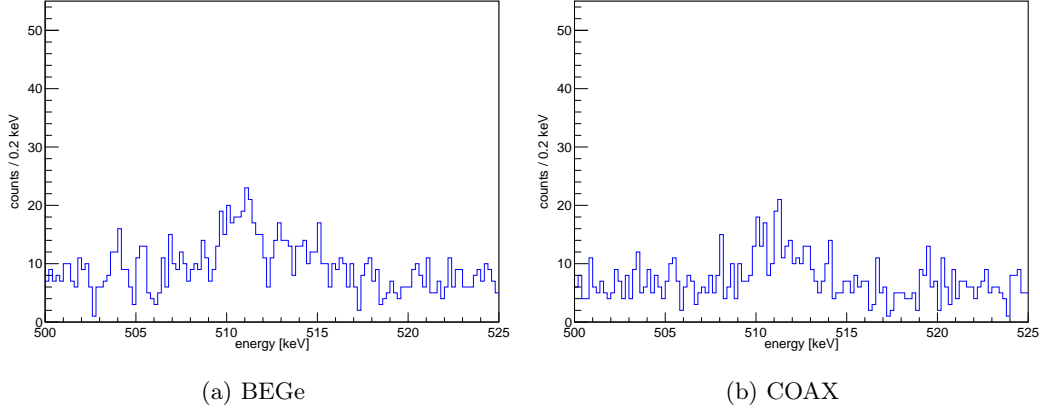


Figure 2.3: Energy spectra showing all events previously rejected by the LAr veto between 500 to 525 keV. The majority of rejected events lie around the 511 keV mark while also a small deviation around the 514 keV mark can be seen.

Another way to possibly single out the  $^{85}\text{Kr}$  decay caused events would be to look for pre-coincidence events in the LAr setup. As the excited  $^{85}\text{Rb}$  nuclei has a half-life of  $1.015\ \mu\text{s}$ , the scintillation light created by the released beta electron is very probable to be measured before the standard veto time frame looking for a coincidental light signal. It should therefore be possible to distinguish  $^{85}\text{Kr}$  decays from other events if one is able to find these incidents.

An investigation to find out whether the pre-coincidence signals are usable was applied by plotting all raw measured LAr veto signals of events with an energy around the 514 keV peak and by manually search for any pre-coincidences. The expected signatures consist of a single peak in the PMTs (for example as seen in Figure 2.4) or a rising edge in the SiPMs respectively. However, this investigation showed that almost none of the events considered had any kind of indication for pre-coincidences. This excludes the presented approach as being a useful  $^{85}\text{Kr}$  indicator.

## 2.3 Spectral Fitting

The spectra from before and after the LAr veto can now be fitted and, from the fit parameters, the amount of measured  $^{85}\text{Kr}$  decay events determined.

The spectra before the LAr vetoes show two peaks in the investigated area. This requires the fit function to include two Gaussian functions from which only the

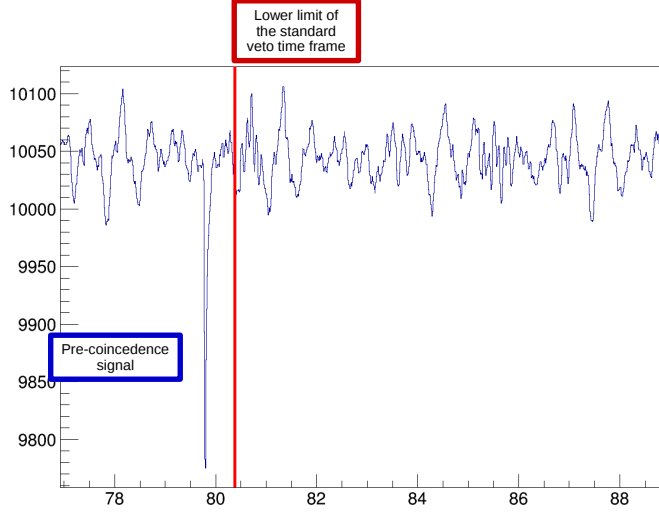


Figure 2.4: The raw signal of photomultiplier tube P4 in event 1614036. The red line shows the lower time window limit for the LAr veto. The pulse which has occurred before the time limit, is probably a pre-coincidence event of a  $^{85}\text{Kr}$  decay via the excited  $^{85m}\text{Rb}$  state.

parameters of the second peak will be used for further analysis. In addition to the two Gaussian peaks, a constant background parameter will be added. Theoretically, the  $^{76}\text{Ge}$  spectra creating this background changes with energy. In the investigated area, however, its overall change is so small that it can be approximated as constant. The resulting fit function is displayed in equation 2.2.

$$f(x) = A \frac{1}{\sqrt{2\pi}C} \exp\left(-\frac{(x-B)^2}{2C^2}\right) + D \frac{1}{\sqrt{2\pi}C} \exp\left(-\frac{(x-E)^2}{2C^2}\right) + F \quad (2.2)$$

Figures 2.5a and 2.5b show the resulting fits. The values of the fit parameter values can be seen in the table inside the figures. Fitting parameters B and E - the mean values of the peaks - were fixed to the values of 511 keV and 514 keV respectively. All other values were left free under the condition of a positive value. Also, parameter C - the sigma value - was used for both peaks. In the energy area investigated, the two resolutions and thus also the variances at the specific energies should not vary greatly, which is why this simplification can be applied. The values determined in the fitting process are compatible with the resolution mentioned earlier.

However, the only fit parameter of real interest in this case is variable D. Its value is the amplitude of the second Gaussian peak. As the Gaussian peak function was

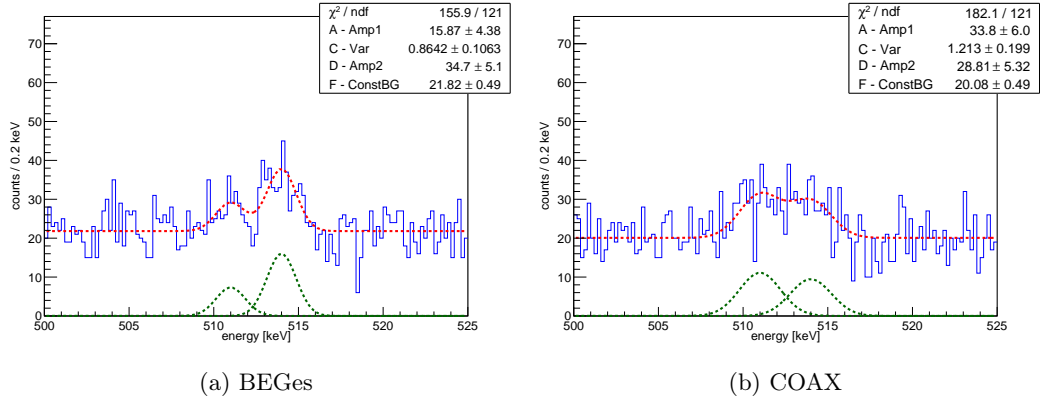


Figure 2.5: Fitted energy spectra before the LAr veto cut between 500 and 525 keV. Function 2.2 was used as fit function and its course is indicated in red. The two green plots at the bottom of the figures indicate the two independent peaks.

already chosen in the normalized form, this value also represents the amount of  $^{85}\text{Kr}$  decays. Taking into account the binning of the histograms, a value of

$$N_{\text{peak,BEGe}} = (183 \pm 25) \text{ cts}$$

in the peak of the BEGe spectrum and

$$N_{\text{peak,COAX}} = (152 \pm 26) \text{ cts}$$

in the COAX spectrum has been determined.

When it comes to the spectrum after the LAr veto, fit function 2.2 will also be used again. This is an advantage because it will also fit around a possible remaining 511 keV peak which otherwise might have affected the outcome. Diagrams 2.6a and 2.6b show the fitted plots. Like above, the amplitude D of the second Gaussian peak corresponds to the number of events measured in the area of the peak per binning. This results in an amount of  $(120 \pm 19)$  counts for the BEGe and  $(128 \pm 22)$  for the COAX spectrum.

Compared to the values of the non LAr filtered spectra, however, it can be seen that the number of counts in the BEGe and in the COAX detectors have dropped considerably. This means that the LAr veto also rejected some of the  $^{85}\text{Kr}$  decay caused events. Therefore only the results of the spectra before the LAr veto will be used in the remaining analysis.

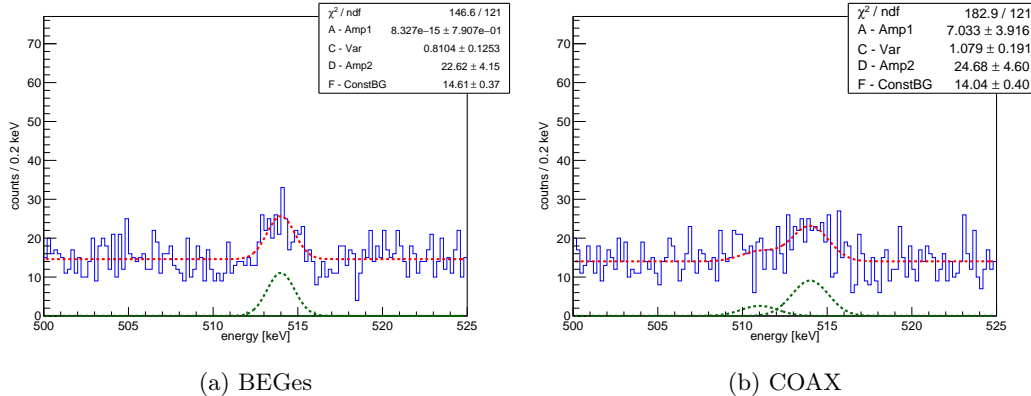


Figure 2.6: Fitted energy spectra after the LAr veto between 500 and 525 keV. Function 2.2 was used as fit function again. In the case of the BEGe spectrum, the first peak function vanishes due to no measurable deviation from the background level at the 511 keV mark. In the COAX spectrum, however, a deviation is still visible which is why the second peak function has a finite amplitude.

## 2.4 Monte Carlo Simulation

It is possible to calculate the decay density of  $^{85}\text{Kr}$  necessary to create the measured line count by using the conversion factor  $1/p\epsilon V_{\text{sim}}$  between these two values. Such a conversion factor can be determined with the help of a Monte Carlo simulation. The tool used to perform this simulation is MAGE (MAjorana-GERda), a GEANT4-based physics simulation software developed jointly by MAJORANA [30] and GERDA. MAGE is specialized in the simulation of radioactive decays and their corresponding energy deposition in germanium detectors. In this thesis, the full GERDA implementation is used [31].

A number of  $N_{\text{sim}} = 50.000.000$  gammas with 514 keV were simulated in cylindrical volume of 2.5 m height and a diameter of 3 m resulting in  $V_{\text{sim}} = 17.65 \text{ m}^3$ . Compared with the volume of  $64 \text{ m}^3$  of the LAr used in the GERDA experiment, this volume is much smaller. Nevertheless, as we will see later, this volume is by far big enough for this purpose.

From these 50 million simulated gammas with the anti-coincidence veto already applied only about 75 thousand have created a signal in a detector, only 30465 of them in a BEGe and 24902 in a COAX detector. The spatial distribution of all measured events in the BEGe detectors can be seen as red dots in Figures 2.7a and 2.7b. Furthermore, the spectrum of all events detected in BEGe detectors is shown

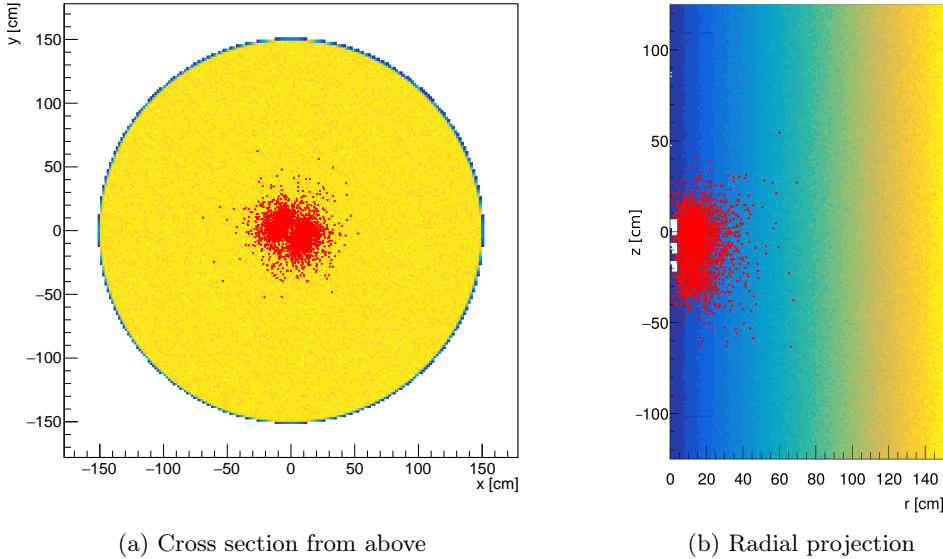


Figure 2.7: The cross section of the simulated volume from above and its radial projection. The colored area shows the density of all simulated decays. The red points indicate all events that were measured by BEGe detectors. It can be seen that gamma emitted far away from the detectors did not produce a measurable signal in the detectors.

in Figure 2.8. One can see that only in a small number of cases the gamma deposited all of its initial 514 keV in the detectors. The majority of photons measured must have scattered before they arrived in the detector or did not deposit all their energy in them. To calculate the detector efficiency, however, only the measured events at the 514 keV peak have to be accounted for. In the BEGe detector spectrum, the peak contains a total of  $\Delta N_{\text{BEGe}} = (4511 \pm 67)$  counts while peak contains  $\Delta N_{\text{COAX}} = (3706 \pm 60)$  in the COAX detectors . With a total of 50 million initial decays, this results in the efficiencies of

$$\epsilon_{\text{BEGe}} = \frac{\Delta N_{\text{BEGe}}}{N_{\text{sim}}} = (9.02 \pm 0.13) \times 10^{-5} \frac{\text{cts}}{\text{gamma}}$$

$$\epsilon_{\text{COAX}} = \frac{\Delta N_{\text{COAX}}}{N_{\text{sim}}} = (7.412 \pm 0.12) \times 10^{-5} \frac{\text{cts}}{\text{gamma}}$$

for the volume of the simulated cylinder. This means that, if a 514 keV photon is emitted at any location in the liquid argon container, it has a probability  $\epsilon_{\text{BEGe}}$  of being measured by one of the BEGe detectors. On the other hand, for every

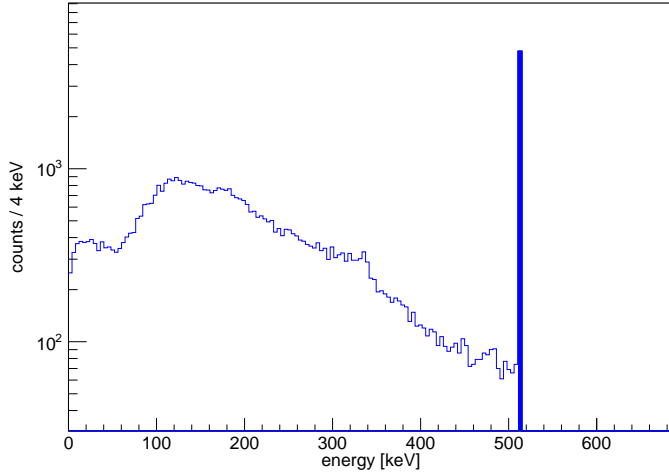


Figure 2.8: Energy spectrum of simulated events measured in BEGe detectors. The blue colored bin represents the counts used for determining the detector efficiency. The majority of measured signals has an energy below 514 keV. Among other things, the Compton peak at roughly 343keV can be seen.

measured 514keV photon in one of the BEGe detectors an average amount of about  $1/\epsilon_{\text{BEGe}} = 10515$  gammas have to be emitted. In other words, the value  $1/\epsilon_{\text{BEGe}}$  is a factor to convert from the amount of measured entries to the average amount of  $^{85m}\text{Rb}$  relaxations necessary to create them.

This value is at volumes big enough direct proportional to the simulated volume  $V_{\text{sim}}$ . This dependency can be derived from Figures 2.7a and 2.7b where the red dots represent the location the measured gamma was released. It can be seen, that essentially all measured gamma originated in the immediate vicinity of the detectors. This would mean that, with a big enough volume and a constant decay density  $\rho_{\text{dec}}$ , the value  $\Delta N$  of each detector remains constant under change of volume.  $N_{\text{sim}}$  on the other hand is directly proportional to the volume through its definition of  $N_{\text{sim}} = \rho_{\text{dec}} V_{\text{sim}}$ . With the definition of the detector efficiency, this results in the proportionality  $1/\epsilon \propto V_{\text{sim}}$ .

Taking this into account, a volume independent conversion factor can be generated by dividing  $1/\epsilon$  through  $V_{\text{sim}}$ . This new value  $1/\epsilon V_{\text{sim}}$  is a conversion factor from the measured line count to the gamma emissions per liter necessary and can also be applied onto the counts measured in the actual LAr tank. By also dividing this new value through the probability  $p = 0.434\%$  gamma/decay, you finally get the desired

conversion factor  $1/p\epsilon V_{\text{sim}}$  between the measured line count and the necessary  $^{85}\text{Kr}$  decay density to generate this peak.

$$\frac{1}{p\epsilon_{\text{BEGe}} V_{\text{sim}}} = (144.65 \pm 2.15) \frac{\text{decay}}{\text{cts} \times 1}$$

$$\frac{1}{p\epsilon_{\text{COAX}} V_{\text{sim}}} = (176.07 \pm 2.90) \frac{\text{decay}}{\text{cts} \times 1}$$

## 2.5 Exposure and Mean Measuring Time

The last remaining value to be determined is the mean measuring time  $\bar{t}$  of all respective detectors. The reason why the whole duration of Phase II cannot be used as measuring time, is due to the fact that not all detectors were recording the entire time. For determining this mean measuring time, the exposures of all individual detectors have to be known. An easy way to determine those values involves the test pulse signal. As mentioned in the introduction, every 20 s the test pulse sends an electric pulse through the front end electronics of the detectors. These events are also recorded and specifically marked as test pulse event.

Due to its periodicity, the effective measurement times of the individual detectors can easily be determined by counting the number of measured test pulse signals in each detector and by multiplying it with the 20 seconds:

$$t_i = N_{\text{TP}}(i) \times 20 \text{ s} \quad (2.3)$$

The masses of the individual detectors are also known. The individual exposures are therefore also easily determinable by applying

$$\varepsilon_i = t_i \times m_i \quad (2.4)$$

The combined exposure of all detectors of the same kind can then be calculated by adding up all of the exposures of the individual detectors.

$$\varepsilon_{\text{comb}} = \sum_i \varepsilon_i \quad (2.5)$$

With this approach, it was possible to determine a combined exposure of  $\varepsilon_{\text{BEGe}} = 30.8 \text{ kg} \cdot \text{yr}$  for the BEGe and  $\varepsilon_{\text{COAX}} = 28.1 \text{ kg} \cdot \text{yr}$  for the COAX. The mean measuring times of the two detector types were then calculated by dividing their combined exposure through their combined masses.

$$\bar{t} = \frac{\varepsilon_{\text{comb}}}{M} = \frac{\sum_i N_{\text{TP}}(i) \times 20 \text{ s} \times m_i}{\sum_i m_i} \quad (2.6)$$

By following this procedure, the mean measuring times for the BEGe and the COAX detectors were determined to be

$$\bar{t}_{\text{BEGe}} = 1.540 \text{ yr}$$

$$\bar{t}_{\text{COAX}} = 1.803 \text{ yr}$$

The simplification of only using the mean measuring time and neglecting the individual detector on/off times creates a systematical error that will be discussed later.

## 2.6 Results

Finally, with the mean measuring times, the line count rates and the conversion factors, the mean specific activity  $\bar{a}$  of  $^{85}\text{Kr}$  over the course of the entire Phase II can be calculated by applying equation 2.1. The resulting mean specific  $^{85}\text{Kr}$  activities are

$$\bar{a}_{\text{BEGe}} = (0.546 \pm 0.083) \frac{\text{mBq}}{\text{l}}$$

$$\bar{a}_{\text{COAX}} = (0.470 \pm 0.089) \frac{\text{mBq}}{\text{l}}$$

These two values differ only inside their range of uncertainty. From these two values an average specific  $^{85}\text{Kr}$  activity for the whole period of Phase II can then be calculated to

$$\bar{a} = (0.508 \pm 0.086) \frac{\text{mBq}}{\text{l}}$$

The uncertainty of this value is only statistical. Systematic errors are caused by the Monte Carlo simulation and the aforementioned on/off time of the detector. The Monte Carlo simulation is able to reproduce the background spectrum, but the complete evaluation of the systematics was not carried out. However, it is assumed that both influences are negligible compared to the current statistical uncertainty.



# **Chapter 3:**

## **Change in Count Rate over Time**

This chapter focuses on the second approach to determine the specific  $^{85}\text{Kr}$  activity based on the change in the total count rate over time. The previous chapter having already determined a value of  $(0.508 \pm 0.086)$  mBq/l for  $^{85}\text{Kr}$ 's specific activity, the purpose of this second approach is to cross-check this value. Because  $^{85}\text{Kr}$  has a half-life of 10.739 yr, a decrease of  $> 10\%$  in its count rate can be expected for a measurement period of about 2 yr.  $^{42}\text{Ar}$  has a similar half-life as  $^{85}\text{Kr}$  (32.9 yr) and, thus, presents the problem that its change should also be measurable [32]. Its possible influence and that of other radioactive isotopes on the count rate is discussed in Section 3.3. For now it will be assumed only  $^{85}\text{Kr}$  should create a visible change. But first, it is necessary to plot the count rate over time to estimate the order of magnitude for the total count rate and for every visible change, as described in Section 3.1. Then, in Section 3.2, a Monte Carlo simulation is used to calculate whether any changes of this scale can occur considering the result of the previous chapter. The last section will focus on fitting exponential decay functions of  $^{85}\text{Kr}$  and  $^{42}\text{Ar}$  through the diagram to determine which isotope may have caused a visible change.

### **3.1 Plotting the Count Rate over Time**

Whether or not  $^{85}\text{Kr}$ 's change is actually visible depends on whether the scale of the total count rate is in the same order of magnitude as  $^{85}\text{Kr}$ 's caused count rate. If the total count rate measured would be in a higher order of magnitude than the change in count rate caused by  $^{85}\text{Kr}$ , its change might not be distinguishable from statistical fluctuation. A considerable portion of the total count rate can be reduced by selecting a suitable upper energy limit, as the influence of radioactive isotopes with a significantly higher Q value than  $^{85}\text{Kr}$ 's can be suppressed by doing so. With the here selected upper limit of 400 keV, only a few  $^{85}\text{Kr}$  events are lost, but the influence of many other radioactive isotopes can be suppressed.

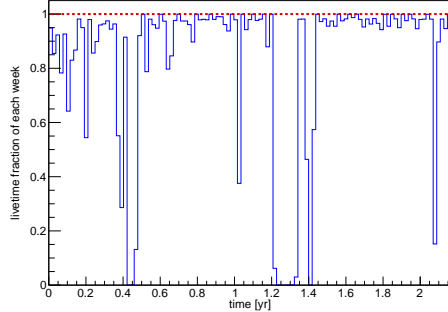


Figure 3.1: The lifetime fractions of the detectors in the respective week plotted over the timeframe between runs 55 and 92.

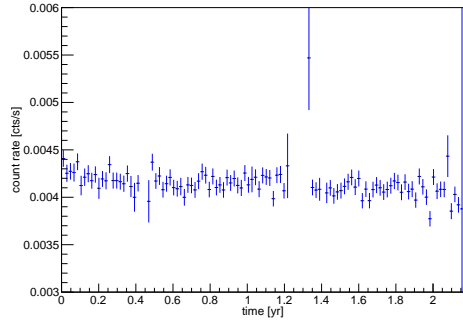


Figure 3.2: Average count rate of each week of events with an energy between 200 to 400 keV plotted over the timeframe between runs 55 and 92.

Additionally, some precautions had to be taken. Together with the upper limit, it is also necessary to set a lower energy limit above the highest energy thresholds present in Phase II. This is done to suppress the influence of changes to the individual detector thresholds on the counting rate and was set to 200 keV. As the count rate is also sensitive to the on/off settings of the detectors, it is necessary that only the data of detectors is used which have always been turned on. For this reason, only the data sets of runs 55 to 92 have been used, as runs 53 and 54 only used a smaller number of detectors. This corresponds to  $41.5 \text{ kg}\cdot\text{yr}$  with BEGe and COAX detectors combined in this analysis. All detectors used for this analysis are listed in table A.1 in the appendix. The standard GERDA analysis cuts have also been applied to this data set.

It is now possible to create a diagram of the total count rates as seen in Figure 3.2. For this purpose, the number of counts measured in each week has to be determined and divided by the measurement time in the same week. The measurement times have to be determined again by counting the number of test pulse signals in each week and by multiplying them by 20 seconds. The lifetime fractions of each week can be seen in Figure 3.1.

The scale of the total count rate in diagram 3.2 is in the order of  $10^{-3} \text{ cts/s}$ . A change in time can be seen from its course.

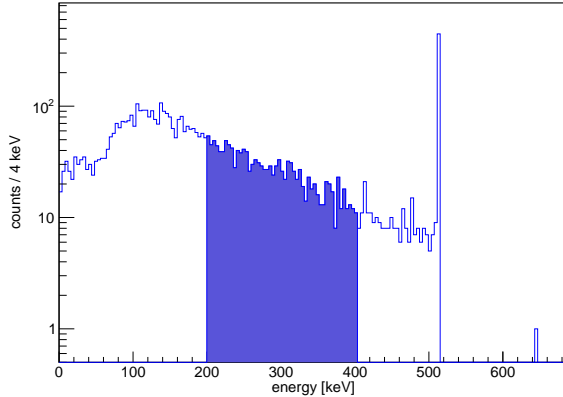


Figure 3.3: Measured energy spectrum of the 1 billion simulated  $^{85}\text{Kr}$  decays. The blue colored area represents the counts used for the calculation of the detector efficiency.

## 3.2 Monte Carlo Simulation

Whether this order of magnitude in the change of the count rate is compatible with the results of the previous chapter must be determined with the aid of a Monte Carlo simulation. With a conversion factor similar to the one derived from the previous simulation, the expected count rate for a given activity of  $^{85}\text{Kr}$  can then be calculated. The difference between the simulations, however, is that, this time, the actual  $^{85}\text{Kr}$  decays are simulated instead of just the 514 keV gamma emissions.

Both betas and gammas contribute at these energies. The range of electrons is only small. Their energy release is strongly influenced by the dead layer implemented in the Monte Carlo simulation. However, this is not the case for the gamma contribution. The source of systematic errors have not been further evaluated. In total  $N_{\text{sim}} = 1$  billion  $^{85}\text{Kr}$  decays have been simulated. From comparison with the previous Monte Carlo simulation a gamma contribution of about 80 % can be estimated.

The colored area of Figure 3.3 contains a number of  $\Delta N = 1438$  counts. This results in a detector efficiency of

$$\epsilon = \frac{\Delta N}{N_{\text{sim}}} = (1.438 \pm 0.038) \times 10^{-6} \frac{\text{cts}}{\text{decay}}$$

Its reciprocal value and its division by the simulated volume result in the volume-independent conversion factor

$$\frac{1}{\epsilon V_{\text{sim}}} = (39.39 \pm 1.04) \frac{\text{decay}}{\text{cts} \times \text{l}}$$

In this case, it can still be assumed that this value is volume-independent, since the beta particles have an even shorter range than the gammas and since the same volume is used as in the previous simulation.

The count rate expected for the previously determined specific activity can now be calculated as follows

$$R_{^{85}\text{Kr}} = \bar{a} \times \epsilon V_{\text{sim}} = (1.29 \pm 0.25) \times 10^{-5} \frac{\text{cts}}{\text{s}}$$

### 3.3 Other Relevant Radioactive Isotopes

If one compares this value with the scale of the count rate diagram above, it can be seen that actually no change caused by  $^{85}\text{Kr}$  should be visible over the statistical fluctuations of the measured count rate. However, the fact that a change can be seen, leaves two possible scenarios. Either the value determined in the first method is wrong and the specific  $^{85}\text{Kr}$  activity in the LAr is actually much higher, or the assumption that  $^{85}\text{Kr}$  was the only isotope with a significant change over time does not hold.

Other isotopes that should be considered are  $^{39}\text{Ar}$  and  $^{42}\text{Ar}$ .  $^{39}\text{Ar}$  is the most active isotope in this energy range, but has a much longer half-life of 269 yr, which means that no change should be visible in the studied time frame [25].  $^{42}\text{Ar}$  has a half-life of 32.9 yr and a Q value in the same energy range as  $^{85}\text{Kr}$  [32], but its specific activity has already been determined to be 0.148 mBq/l [33]. Moreover  $^{42}\text{Ar}$ , unlike  $^{85}\text{Kr}$  has no gamma contribution. Due to the significantly lower efficiency of the detectors to detect beta in this energy range, as it has been shown from the comparison of the two Monte Carlo simulations, no change generated by this isotope should be detectable. However, its also unstable daughter nucleus  $^{42}\text{K}$  is positively charged right after its creation and is therefore not homogeneously distributed. This results in a much higher  $^{42}\text{K}$  density around the detectors and therefore a higher measurable specific activity. As  $^{42}\text{K}$  has a much lower half-life than  $^{42}\text{Ar}$ , any change in  $^{42}\text{Ar}$ 's activity also changes the  $^{42}\text{K}$ 's activity. This means  $^{42}\text{Ar}$ 's change over time gets effectively amplified in the count rate diagram to a level that it could

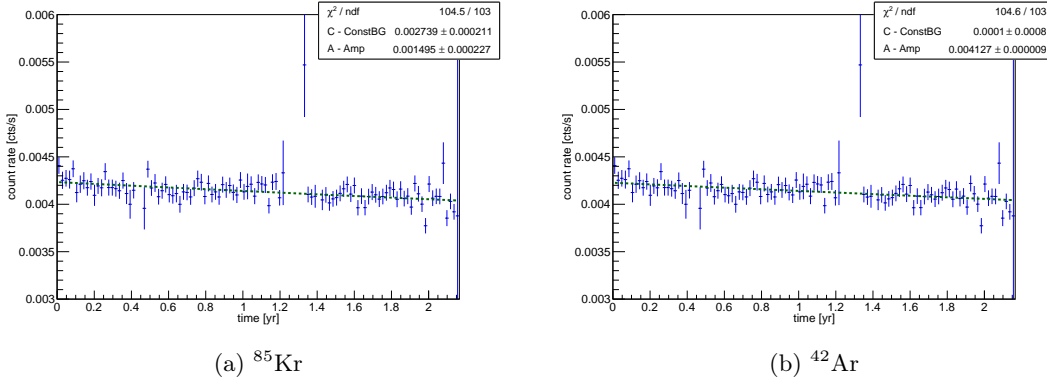


Figure 3.4: Fitted count rate graph using function 3.1 with parameter B fixed on the half-lives of the respective radioactive isotope.

possibly cause the change seen.

### 3.4 Count Rate Fitting

To find out whether the change was caused by  $^{85}\text{Kr}$  or  $^{42}\text{Ar}$ , it is necessary to fit plot 3.1 with the respective exponential decay functions of the two isotopes. The goodness of the fits might allow to disentangle the two isotopes. Function 3.1 was used for the fits with parameter B fixed to the respective half-lives of the two isotopes.

$$f(x) = A \times \exp\left(-\frac{\log(2)}{B}x\right) + C \quad (3.1)$$

The resulting fitting plots can be seen in Figures 3.4a and 3.4b. From the resulting amplitude in the  $^{85}\text{Kr}$  fit, a specific activity of  $(58.9 \pm 10.5) \text{ mBq/l}$  can be calculated using the conversion factor. This value is, as expected, much higher than determined in the previous chapter. For  $^{42}\text{Ar}$  no Monte Carlo simulation was available. Its non-homogeneous distribution makes it difficult.

Concerning the goodness of the fit, the chi-squared  $\chi^2$  value of the two fit functions can be evaluated. The smaller this value, the better the fit function describes the measured data. However, in this case, both fit functions seem to have a similar  $\chi^2$  value and therefore describe the course of the data equality well. This leads to the conclusion that the data used in this method is not informative enough to be able to discriminate which of the two isotopes is responsible for the change. Therefore,

no statement can be made about the specific activity of  $^{85}\text{Kr}$  from this change in count rate. With a measurement time in the order of magnitude of the half-life of the isotopes, it may be feasible to make a statement about the isotope responsible and possibly to also falsify the result from the previous chapter.

Since  $^{42}\text{K}$  has a much higher Q value ( $Q_\beta = 3525.22 \text{ keV}$  [32]) than  $^{85}\text{Kr}$ , it should be possible to choose another energy frame above  $^{85}\text{Kr}$ 's Q-value and to determine its change in the count rate there without  $^{85}\text{Kr}$ 's influence.

# Chapter 4:

## Conclusion, Comparison and Outlook

### 4.1 Conclusion

With the line count rate analysis, it was possible to show that the specific activity of  $^{85}\text{Kr}$  in the LAr in GERDA Phase II has a value of  $(0.508 \pm 0.086)$  mBq/l. The attempt to verify this number using the half-life did not give an answer. Due to  $^{85}\text{Kr}$ 's low value, only a strong discrepancy could have been detected. However, the presence of  $^{42}\text{Ar}$  with a similar decay time and its daughter nuclei  $^{42}\text{K}$  did not allow to confirm or falsify the value of the previous method.

### 4.2 Comparison to WARP and Darkside

Two other experiments, also using LAr, were mentioned at the end of the introduction chapter: the Darkside experiment using UAr and the WARP experiment also using argon from the atmosphere. It was assumed earlier that Darkside's specific  $^{85}\text{Kr}$  activity was two orders of magnitude smaller than in the WARP experiment as the UAr did not come into contact with the man-made  $^{85}\text{Kr}$ . Surprisingly, however, GERDA measured a much lower specific  $^{85}\text{Kr}$  activity than WARP or Darkside while also using argon originating from the atmosphere.

Besides the activities themselves, one could also chose an alternative way and calculate how high the line count would have been in the GERDA setup if the specific activities of WARP and Darkside were present. In Section 2.3 a line count of about 180 counts was found at 514 keV. The corresponding line count from the specific activities of the other experiments can then be determined by upscaling the line count measured in GERDA to the corresponding values with the factor  $(\bar{a}_{\text{Exp}}/\bar{a}_{\text{GERDA}})$ . This results in a line count of about  $\mathcal{O}(1000)$  cts in the Darkside experiment and about  $\mathcal{O}(50000)$  cts in the WARP experiment, which means, that a much higher peak could have been measured.

Moreover, one can now also determine the expected count rate from the second method. Since the specific  $^{85}\text{Kr}$  activity of Darkside is only one order of magnitude

higher than that of GERDA, one should hardly see any change here either. On the other hand, one can calculate an expected count rate for WARP in the order of  $10^{-3}$  cts/s, so in this case a significant change should be recognizable.

To gain further insight into why the specific  $^{85}\text{Kr}$  activity in GERDA can be so much lower, one could study the purification process during filling of the GERDA cryostat before starting with Phase I. Also the source of the argon might be of interest as in the higher levels of the atmosphere the  $^{85}\text{Kr}$  concentration is relatively homogeneous [34] but at lower levels strongly dependent on the proximity to a nuclear fission reactor [35].

### 4.3 Outlook

Also mentioned in the introduction, the GERDA experiment is planned to keep measuring until 2020. Afterwards the GERDA setup will be converted into the LEGEND experiment that will further investigate the  $0\nu\beta\beta$  decay in  $^{76}\text{Ge}$  and will use a new LAr filling. It is therefore possible that in LEGEND a much higher concentration of  $^{85}\text{Kr}$  may be present and, thus, the radioactive background in the lower energy range may be larger. This would result in a much higher contribution of  $^{85}\text{Kr}$  to the background of any low energy analysis.

## **Appendix A:**

### **Detector Overview**

In order to determine the specific  $^{85}\text{Kr}$  activity in the second method, only the data of the detectors that have been turned on during the entire time could be used. Table A.1 lists all detectors and shows whether they have continuously recorded data from runs 53 to 92 or from 55 to 92. In the final analysis, only the data sets of runs 55 to 92 were used, as during this time set more detectors have been continuously measuring, which results in a higher exposure ( $41.5 \text{ kg} \cdot \text{yr}$ ) compared to the alternative ( $21.9 \text{ kg} \cdot \text{yr}$ ).

Channel	Type	53-92	55-92	Channel	Type	53-92	55-92
0	BEGe	X	X	20	BEGe	X	X
1	BEGe	X	X	21	BEGe	X	X
2	BEGe	X	X	22	BEGe	X	X
3	BEGe		X	23	BEGe		
4	BEGe		X	24	BEGe	X	X
5	BEGe			25	BEGe		
6	BEGe			26	BEGe		
7	BEGe			27	COAX		
8	COAX		X	28	COAX		X
9	COAX		X	29	COAX	X	X
10	COAX	X	X	30	BEGe	X	X
11	BEGe	X	X	31	BEGe		X
12	BEGe		X	32	BEGe		
13	BEGe			33	BEGe		
14	BEGe	X	X	34	BEGe		
15	BEGe			35	BEGe		
16	BEGe			36	COAX		
17	BEGe	X	X	37	natural		
18	BEGe		X	38	natural		
19	BEGe	X	X	39	natural		

Table A.1: Detector overview. It indicates which detectors have continuously been switched on during the runs 53 to 92 or 55 to 92 by placing an X in the respective box.

# Bibliography

- [1] J. Schechter and J. W. F. Valle. »Neutrinoless double- decay in SU(2)U(1) theories«. en. In: *Physical Review D* 25.11 (June 1982), pp. 2951–2954. ISSN: 0556-2821. DOI: 10.1103/PhysRevD.25.2951. URL: <https://link.aps.org/doi/10.1103/PhysRevD.25.2951> (visited on 04/08/2018).
- [2] S. M. Bilenky and S. T. Petcov. »Massive neutrinos and neutrino oscillations«. In: *Rev. Mod. Phys.* 59.3 (July 1987), pp. 671–754. DOI: 10.1103/RevModPhys.59.671. URL: <https://link.aps.org/doi/10.1103/RevModPhys.59.671> (visited on 06/08/2018).
- [3] M. Agostini et al. »Background free search for neutrinoless double beta decay with GERDA Phase II«. In: *Nature* 544.7648 (Apr. 2017). arXiv: 1703.00570, pp. 47–52. ISSN: 0028-0836, 1476-4687. DOI: 10.1038/nature21717. URL: <http://arxiv.org/abs/1703.00570> (visited on 04/08/2018).
- [4] Y. Fukuda et al. »Evidence for Oscillation of Atmospheric Neutrinos«. en. In: *Physical Review Letters* 81.8 (Aug. 1998), pp. 1562–1567. ISSN: 0031-9007, 1079-7114. DOI: 10.1103/PhysRevLett.81.1562. URL: <https://link.aps.org/doi/10.1103/PhysRevLett.81.1562> (visited on 04/08/2018).
- [5] SNO Collaboration et al. »Direct Evidence for Neutrino Flavor Transformation from Neutral-Current Interactions in the Sudbury Neutrino Observatory«. In: *Phys. Rev. Lett.* 89.1 (June 2002), p. 011301. DOI: 10.1103/PhysRevLett.89.011301. URL: <https://link.aps.org/doi/10.1103/PhysRevLett.89.011301> (visited on 06/08/2018).
- [6] J. Shirai. »Double Beta Decay«. In: *Int. J. Mod. Phys. Conf. Ser.* 46 (Jan. 2018), p. 1860002. DOI: 10.1142/S2010194518600029. URL: <https://www.worldscientific.com/doi/abs/10.1142/S2010194518600029> (visited on 04/08/2018).
- [7] A. S. Barabash. »Brief review of double beta decay experiments«. In: *arXiv:1702.06340 [nucl-ex]* (Feb. 2017). arXiv: 1702.06340. URL: <http://arxiv.org/abs/1702.06340> (visited on 04/08/2018).
- [8] S. Dell’Oro et al. »Neutrinoless double beta decay: 2015 review«. In: *Advances in High Energy Physics* 2016 (2016). arXiv: 1601.07512, pp. 1–37. ISSN: 1687-7357, 1687-7365. DOI: 10.1155/2016/2162659. URL: <http://arxiv.org/abs/1601.07512> (visited on 04/08/2018).

- [9] S. M. Bilenky, F. Capozzi and S. T. Petcov. »An alternative method of determining the neutrino mass ordering in reactor neutrino experiments«. In: *Physics Letters B* 772 (Sept. 2017), pp. 179–183. ISSN: 0370-2693. DOI: 10.1016/j.physletb.2017.06.044. URL: <http://www.sciencedirect.com/science/article/pii/S0370269317305208> (visited on 04/08/2018).
- [10] E. W. Otten and C. Weinheimer. »Neutrino mass limit from tritium beta decay«. In: *Reports on Progress in Physics* 71.8 (Aug. 2008). arXiv: 0909.2104, p. 086201. ISSN: 0034-4885, 1361-6633. DOI: 10.1088/0034-4885/71/8/086201. URL: <http://arxiv.org/abs/0909.2104> (visited on 04/08/2018).
- [11] K. N. Abazajian et al. »Cosmological and Astrophysical Neutrino Mass Measurements«. In: *Astroparticle Physics* 35.4 (Nov. 2011). arXiv: 1103.5083, pp. 177–184. ISSN: 09276505. DOI: 10.1016/j.astropartphys.2011.07.002. URL: <http://arxiv.org/abs/1103.5083> (visited on 04/08/2018).
- [12] S. M. Bilenky and C. Giunti. »Neutrinoless Double-Beta Decay: a brief Review«. en. In: *Modern Physics Letters A* 27.13 (Apr. 2012), p. 1230015. ISSN: 0217-7323, 1793-6632. DOI: 10.1142/S0217732312300157. URL: <http://www.worldscientific.com/doi/abs/10.1142/S0217732312300157> (visited on 04/08/2018).
- [13] Steven R. Elliott and Petr Vogel. »Double Beta Decay«. In: *Annual Review of Nuclear and Particle Science* 52.1 (2002), pp. 115–151. DOI: 10.1146/annurev.nucl.52.050102.090641. URL: <https://doi.org/10.1146/annurev.nucl.52.050102.090641> (visited on 24/07/2018).
- [14] M. Agostini et al. »The background in the  $0\nu\beta\beta$  experiment Gerda«. en. In: *Eur. Phys. J. C* 74.4 (Apr. 2014), p. 2764. ISSN: 1434-6044, 1434-6052. DOI: 10.1140/epjc/s10052-014-2764-z. URL: <https://link.springer.com/article/10.1140/epjc/s10052-014-2764-z> (visited on 25/07/2018).
- [15] M. Agostini et al. »Production, characterization and operation of  $^{76}\text{Ge}$  enriched BE Ge detectors in GERDA«. en. In: *Eur. Phys. J. C* 75.2 (Feb. 2015), p. 39. ISSN: 1434-6044, 1434-6052. DOI: 10.1140/epjc/s10052-014-3253-0. URL: <https://link.springer.com/article/10.1140/epjc/s10052-014-3253-0> (visited on 26/07/2018).
- [16] M. Agostini et al. »Pulse shape discrimination for Gerda Phase I data«. en. In: *Eur. Phys. J. C* 73.10 (Oct. 2013), p. 2583. ISSN: 1434-6044, 1434-6052. DOI: 10.1140/epjc/s10052-013-2583-7. URL: <https://link.springer.com/article/10.1140/epjc/s10052-013-2583-7> (visited on 30/07/2018).

- [17] S. Riboldi et al. »Cryogenic readout techniques for Germanium detectors«. In: IEEE, Apr. 2015, pp. 1–6. ISBN: 978-1-4799-9918-7. DOI: 10.1109/ANIMMA.2015.7465549. URL: <http://ieeexplore.ieee.org/document/7465549/> (visited on 04/08/2018).
- [18] Gerda Collaboration et al. »Upgrade for Phase II of the Gerda experiment«. en. In: *Eur. Phys. J. C* 78.5 (May 2018), p. 388. ISSN: 1434-6044, 1434-6052. DOI: 10.1140/epjc/s10052-018-5812-2. URL: <https://link.springer.com/article/10.1140/epjc/s10052-018-5812-2> (visited on 21/07/2018).
- [19] Anna Julia Zsigmond. »New Results From Gerda Phase II«. In: (June 2018). DOI: 10.5281/zenodo.1287604. URL: <https://zenodo.org/record/1287604> (visited on 04/08/2018).
- [20] Kevin S Olsen. »Improvements to the resolution and efficiency of the DEAP-3600 dark matter detector and their effects on background studies«. en. PhD thesis. University of Alberta.
- [21] J. Janicskó Csáthy et al. »Optical fiber read-out for liquid argon scintillation light«. In: *arXiv:1606.04254 [hep-ex, physics:physics]* (June 2016). arXiv: 1606.04254. URL: <http://arxiv.org/abs/1606.04254> (visited on 25/07/2018).
- [22] Matteo Agostini et al. »GELATIO: A general framework for modular digital analysis of high-purity Ge detector signals«. In: *Journal of Instrumentation - J INSTRUM* 6 (June 2011). DOI: 10.1088/1748-0221/6/08/P08013.
- [23] Matteo Agostini, Luciano Pandola and Paolo Zavarise. »Off-line data processing and analysis for the GERDA experiment«. In: *Journal of Physics: Conference Series* 368 (Nov. 2011). DOI: 10.1088/1742-6596/368/1/012047.
- [24] *Decay Scheme*. URL: [http://www.nndc.bnl.gov/chart/getdecayscheme.jsp?nucleus=85RB&dsid=85kr%20bM%20decay%20\(10.739%20y\)&unc=nds](http://www.nndc.bnl.gov/chart/getdecayscheme.jsp?nucleus=85RB&dsid=85kr%20bM%20decay%20(10.739%20y)&unc=nds) (visited on 06/08/2018).
- [25] Balraj Singh and Jun Chen. »Nuclear data sheets for A = 85«. English (US). In: *NUCL.DATA SHEETS SER. B, NUCL.DATA SHEETS SER.B, NUCL.DATA SHEETS SER.B*. 116.1 (2014), pp. 1–162. ISSN: 0090-3752. DOI: 10.1016/j.nds.2014.01.001. URL: <https://scholars.opb.msu.edu/en/publications/nuclear-data-sheets-for-a-85> (visited on 19/07/2018).
- [26] Jochen Ahlswede et al. »Update and improvement of the global krypton-85 emission inventory«. In: *Journal of Environmental Radioactivity* 115 (Jan. 2013), pp. 34–42. ISSN: 0265-931X. DOI: 10.1016/j.jenvrad.2012.07.006. URL: <http://www.sciencedirect.com/science/article/pii/S0265931X12001816> (visited on 30/07/2018).

- [27] K. Winger et al. »A new compilation of the atmospheric 85krypton inventories from 1945 to 2000 and its evaluation in a global transport model«. In: *Journal of Environmental Radioactivity* 80.2 (Jan. 2005), pp. 183–215. ISSN: 0265-931X. DOI: 10.1016/j.jenvrad.2004.09.005. URL: <http://www.sciencedirect.com/science/article/pii/S0265931X04002887> (visited on 30/07/2018).
- [28] P. Agnes et al. »Results from the first use of low radioactivity argon in a dark matter search«. In: *Phys. Rev. D* 93.8 (Apr. 2016), p. 081101. DOI: 10.1103/PhysRevD.93.081101. URL: <https://link.aps.org/doi/10.1103/PhysRevD.93.081101>.
- [29] P Benetti et al. »Measurement of the specific activity of Ar-39 in natural argon«. In: *Nuclear Instruments and Methods in Physics Research Section A Accelerators Spectrometers Detectors and Associated Equipment* 574 (Apr. 2006). DOI: 10.1016/j.nima.2007.01.106.
- [30] C. E. Aalseth et al. »Search for Zero-Neutrino Double Beta Decay in  $^{76}\text{Ge}$  with the Majorana Demonstrator«. In: *Physical Review Letters* 120.13 (Mar. 2018). arXiv: 1710.11608. ISSN: 0031-9007, 1079-7114. DOI: 10.1103/PhysRevLett.120.132502. URL: <http://arxiv.org/abs/1710.11608> (visited on 06/08/2018).
- [31] Melissa Boswell et al. »MaGe - a Geant4-based Monte Carlo Application Framework for Low-background Germanium Experiments«. In: *IEEE Transactions on Nuclear Science* 58.3 (June 2011). arXiv: 1011.3827, pp. 1212–1220. ISSN: 0018-9499, 1558-1578. DOI: 10.1109/TNS.2011.2144619. URL: <http://arxiv.org/abs/1011.3827> (visited on 04/08/2018).
- [32] Jun Chen and Balraj Singh. »Nuclear Data Sheets for  $A = 42$ «. In: *Nuclear Data Sheets* 135 (July 2016), pp. 1–192. ISSN: 0090-3752. DOI: 10.1016/j.nds.2016.06.001. URL: <http://www.sciencedirect.com/science/article/pii/S0090375216300126> (visited on 20/07/2018).
- [33] Neslihan Becerici Schmidt. »Results on Neutrinoless Double Beta Decay Search in GERDA: Background Modeling and Limit Setting«. PhD thesis. Technische Universität München, June 2014. URL: [https://www.mpi-hd.mpg.de/gerda/public/2014/phd2014\\_neslihanBecericiSchmidt.pdf](https://www.mpi-hd.mpg.de/gerda/public/2014/phd2014_neslihanBecericiSchmidt.pdf) (visited on 20/07/2018).
- [34] Daniel J. Jacob et al. »Atmospheric distribution of  $^{85}\text{Kr}$  simulated with a general circulation model«. In: *Journal of Geophysical Research* 92 (June 1987), pp. 6614–6626. DOI: 10.1029/JD092iD06p06614.

- [35] W. Weiss et al. »Mesoscale transport of  $^{85}\text{Kr}$  originating from European sources«. In: *Nuclear Instruments and Methods in Physics Research Section B: Beam Interactions with Materials and Atoms* 17.5 (Nov. 1986), pp. 571–574. ISSN: 0168-583X. DOI: 10.1016/0168-583X(86)90216-8. URL: <http://www.sciencedirect.com/science/article/pii/0168583X86902168> (visited on 30/07/2018).